PHYSICAL REVIEW B **101**, 224101 (2020)

Experimental evidence for the elastic long-range character of the spin crossover transition in cooperative single crystals

Houcem Fourati and Kamel Boukheddaden*
Université Paris-Saclay, UVSQ, Groupe d'Etudes de la Matière Condensée, UMR CNRS No. 8635, 45 Avenue des Etats Unis, 78035 Versailles, France

(Received 23 December 2019; revised manuscript received 18 March 2020; accepted 13 May 2020; published 1 June 2020)

We evidenced by means of optical microscopy the long-range character of the interactions acting in spin crossover (SCO) single crystals through a study of the optical density (OD) variation during the spin transition between high-spin (HS) and low-spin (LS) states. The time evolution of the local OD, measured in four single crystals, revealed the existence of precursor phenomena, which are manifest through the appearance of significant changes in the OD of the probed area well before the arrival of the front interface in the case of HS to LS transition and after the passage of the interface in the case of LS to HS transition. These two effects are attributed to the manifestation of long-range interactions that develop during the propagation of the HS/LS interface, which is accompanied by a volume change, generating elastic stresses in the material that deploy far from the sources. Interestingly, the experimental investigations indicate that the precursor and the after effect phenomena occur mostly in the HS phase, which is softer than the LS phase. These original experimental results are well reproduced using an electroelastic modeling in which we considered, in addition to the lattice misfit between HS and LS states, the existence of different elastic constants in the HS and LS phases.

DOI: 10.1103/PhysRevB.101.224101

I. INTRODUCTION

Bistability in spin crossover (SCO) materials is a typical physical property of switchable molecular solids that promises many applications as materials for information storage, sensor displays, or spintronics [1–7]. SCO solids have been studied for a long time [8–12], and Fe(II)-based SCO systems are the most popular in this field. In this case, bistability occurs between the high-spin (HS) state where the spin moment has the maximum value $S = 2$ ($t_{2g}^4 e_g^2$), and the low-spin (LS) state where the total spin is $S = 0$ ($t_{2g}^6 e_g^0$). According to the strength of the ligand field, $\Delta = E(t_{2g}) - E(e_g)$, the metal ion can be in the LS (HS) state when Δ is much stronger (weaker) than the electron pairing energy. The resulting spin state then emerges from the delicate balance between the orbital energy needed to occupy all of the 3d levels in order to maximize the spin state and the average energy of the Coulomb repulsion of the d-electrons. Various external stimuli, such as temperature, pressure, light [9,13–16], etc., can trigger the spin transition of SCO compounds.

In the solid state, the thermal properties of SCO materials gives rise to a rich variety of behaviors, ranging from (i) a simple continuous gradual spin transition corresponding to a Boltzmann population of two degenerate states to (ii) sharp first-order transitions, including (iii) incomplete transitions, with the presence of a nonzero residual HS fraction at low-temperature, and (iv) two-step or multistep spin transitions, characterized by the presence of a macroscopic intermediate state over the course of the transition between the LS and the HS states [17–21]. From the microscopic point of view, the spin transition is intrinsically a vibronic problem [22–25] in which the electronic and vibrational structures of the molecule are strongly intricate. The change of the magnetic state of the metal centers is accompanied by local volume changes at the molecular level, which delocalize far from the epicenters of the transformations (long-range interaction), a result of the elastic interactions between the SCO units, leading to a macroscopic volume change stabilizing the LS and HS phases at low and high temperature, respectively. These electronic and elastic changes cause significant changes in the physical properties, such as color, mechanical properties, etc. The investigations of this phenomenon can be monitored by a variety of experimental techniques, including x-ray diffraction [26], Mössbauer spectroscopy [27], optical microscopy (OM) [28–39], and calorimetry [40].

Long-range interactions play an important role in the cooperative character of SCO systems, as was demonstrated theoretically [41–47], since they are at the origin of domain formation of the macroscopic coexistence of HS and LS phases. From an experimental point of view, the OM technique was used to study various single crystals performing first-order phase transitions. In all of them, the spin transition occurred through a nucleation and propagation process with the presence of a clear interface between the LS and HS states [28–38]. These experimental observations have been reproduced theoretically using electroelastic models [34,43,48–50], taking into account the system volume change at the transition. Electroelastic models that combine spin state changes and lattice position displacements are highly efficient in the

---

[*] kamel.boukheddaden@uvsq.fr

description of the main features of SCO materials, although they are solved by Monte Carlo (MC) simulations, whose timescale is clearly different from that of the experiment.

In the present work, from an experimental point of view, we demonstrate the effect of long-range interactions using the OM technique via an analysis of the optical density (OD) changes before and after the phase boundary. This work is realized on four single crystals belonging to three SCO compounds, with the objective to demonstrate the general character of this phenomenon. Very recently, Fourati *et al.* [35,36] studied by OM two cooperative SCO single crystals, namely $[\{Fe(2\text{-pytrz})_2[Pd(CN)_4]\}]\cdot 3H_2O$ and $[\{Fe(2-\text{pytrz})_2[Pt(CN)_4]\}]\cdot 3H_2O$, denoted here as compounds **1** and **2**, which showed first-order phase transitions accompanied with well-defined interfaces during the spin transition process. On the other hand, the resilient character of these two investigated single crystals allowed us to prove the relation between the shape of the HS-LS interface and the macroscopic crystal's shape. There, the interplay between the crystal and interface shapes has been studied extensively, and the obtained results were very well reproduced by a reaction diffusion model [35,36,51].

The present investigations are also performed on the compound $[\{Fe(NCSe)(py)_2\}_2(m\text{-bpypz})]$ [34,37,50,52], denoted here as compound **3**. This system has already showed its robust character since it was possible to follow reversibly by OM the propagation of the HS/LS front interface along the cooling and heating branches of its thermal hysteresis, without any damage. The velocities of the front propagation were estimated in the interval 4–6 μms^{-1}. Due to the regular form of the crystal, as elongated platelets along the direction of the interface propagation, the shape of the HS/LS interface remains invariant along the spin transition process. From a theoretical point of view, the long-range character of the spin transition phenomenon was proposed by Nishino *et al.* [43], who demonstrated the macroscopic character of the nucleation and growth phenomena in SCO lattices, and explained its origin as due to the macroscopic lattice deformation accompanying the spin transition. Here we aim to demonstrate experimentally by means of OM experiments the long-range character of the SCO phenomenon. Toward that end, several SCO single crystals have been reinvestigated by focusing on the time dependence of the local OM signal at a selected region at which we probe the change of the elastic properties resulting from the front propagation. The manuscript is organized as follows: in Sec. II, we present the experimental results of OM, Sec. III, contains the theoretical part of this study, and in Sec. IV we conclude and outline some possible developments of this work.

II. PROPAGATION OF THE HS-LS PHASE BOUNDARY

Optical microscopy setup

OM investigations were performed in a transmission mode using a standard optical microscope Nikon Eclipse LV100 equipped with a fast CCD camera (DALSA Falcon 1.4M100HG Color, 100fps max) and adapted to cryogenic experiments [35,38]. We automatically recorded the PC screen by using CAMSTUDIO software. For obtaining complete images of the crystal, we used an objective X20 (numerical aperture NA = 0.4), leading to a resolution limit of 0.3 μm. The experiment in the current manuscript consists of recording the crystal's images as a function of temperature or on time at a constant temperature in transmission geometry using backward illumination by a tungsten halogen lamp, provided by the microscope. It is important to note that the microscope light was shone on the whole crystal.

Data analysis

The image data are extracted as a set of three matrices, associated with the red, green, and blue (R, G, B) components of the intensity of light. Such coding can be done in TIFF or JPEG format and the images are conveniently treated numerically with the MATLAB package. The camera data can also be saved in the form of AVI movies, which require less memory space and can be converted into JPEG images using VIRTUALDUB software. The region of the crystal between facets perpendicular to the microscope axis will provide quantitative data through the analysis of the optical densities (ODs) defined as the ratio $\text{OD} = \log_{10}(I_{\text{incident}}/I_{\text{transmitted}})$ [OD is proportional to absorbance, $A = \ln(I_{\text{incident}}/I_{\text{transmitted}})$]. With a color camera, red, green, and blue intensity data are obtained independently, and their incident values are easily determined from the bright field background. In the MATLAB program, we select some region of the image outside the crystal corresponding to the bright field ($\simeq 100$ pixels) and we average the pixel intensity. This value represents I_{incident}. In the second step, we select another region of the image situated on the crystal, and here it can be either some local part of the crystal or the whole crystal. We also average the pixel intensity, and this is denoted by the value $I_{\text{transmitted}}$. This process is applied for every image during the analysis.

The cryogenic OM technique is used here to visualize the spatiotemporal aspects of the spin transition in SCO single crystals [28–38]. All of the studied SCO compounds undergo a first-order phase transition between the LS and HS states and are characterized by their color change during the spin transition, allowing the use of image processing for the data treatment. The variation of the transmitted intensity, I, of light through the crystal is related to the OD [35,36,38], which is defined as the decimal logarithm of the ratio of incident/transmitted intensities,

$$\text{OD} = \log_{10}\frac{I_0}{I}. \tag{1}$$

In the transmission geometry, I_0 is merely the bright field intensity, and I can be determined, either locally or on average, over a defined area of the crystal. In general, the description of the thermal properties of SCO systems is done with the common local $[n_{\text{HS}}(x,y)]$ or average (n_{HS}) order parameter, i.e., the HS fraction, corresponding to the fraction of molecules in the HS state, and which connects to the normalized local OD as follows:

$$n_{\text{HS}} = \frac{\text{OD}(x,y) - \text{OD}_{\text{HS}}}{\text{OD}_{\text{HS}} - \text{OD}_{\text{LS}}}, \tag{2}$$

where OD_{HS} and OD_{LS} are, respectively, the OD values in the HS and LS states. According to the existence of three OD signals associated with the blue, green, and red pixels, three

HS fractions can be extracted from the data. Depending on the single-crystal thickness and color, from one compound to another, the signal quality (signal-to-noise ratio) would perhaps be better, either in the red, green, or the blue pixel. The OM data (recorded images) were treated using MATLAB programs developed in the Versailles group [38]; each image was split into three OD components: red, green, and blue.

Precursor and after-effect phenomena

The mechanical properties of the crystal are impacted by the process of nucleation and growth of the HS/LS interface due to the long-range nature of the elastic interactions, which take place through the volume change accompanying the spin transition. The present investigations focus on the local evolution of the OD, evaluated in selected small square-shaped areas of $2 \times 2\ \mu\mathrm{m}^2$ situated in the direction of propagation of the front transformation. This small region is then used to probe the local optical changes of the single crystal along cooling and heating regimes.

It is worth noting that the choice of a small crystal's area as a probe is motivated by the enhanced sensitivity of detection to local OD changes, while the sensitivity of the local changes decreases significantly if one considers the spatially averaged OD response of the whole crystal. Of course, one can select several small regions situated in front of the interface to obtain statistics on their resulting behavior. This method is interesting for straight interfaces moving at constant velocity reaching the probed regions simultaneously (synchronously). This is difficult to achieve in practice in most of the SCO single crystals due to their irregular shapes, which perturb the velocity and the shape of the interfaces. Another difficulty comes from the possible variation of the crystal thickness from one point to another, affecting the OD, which may preclude the desired effect. So, the objective here is to provide a spatiotemporal map of the deployment of the strain along the front propagation process. This information cannot be obtained from the dependence of the average HS fraction.

Single crystals (**1**) [35] are presented with different shapes: rectangular (**1a**) and triangular (**1b**). Figure 1 summarizes the results of the OM investigations on the single crystal **1a**. The corresponding thermal behavior of the HS fraction, presented in Fig. 1(a), is derived from the thermal dependence of the green OD shown in Fig. S1b [53] using Eq. (2). The green pixels showed the best noise-to-signal ratio compared to those of the red and blue OD pixels [the behaviors are shown in Figs. S1a and S1c of the supplemental material (SM) [53]]. The thermal behavior of the HS fraction indicates transition temperatures of $T \simeq 153$ K and $T \simeq 163$ K for the cooling and heating processes, respectively. As mentioned in the Introduction, the spin transition is accompanied by a global volume change, as clearly confirmed by the data of Fig. 1(b), where we have indicated the different lengths of the studied single crystal in both spin states (HS state and LS state). All length measurements ($\simeq$ hundred of microns) derived from the present OM studies were obtained using IMAGEJ software, with systematic error bars of the order of magnitude of the pixel, i.e., $\sim 0.3\ \mu$m. The macroscopic relative size variations, estimated to be 1.4–2.2 % by OM, are in good agreement with those derived from x-ray diffraction data, which indicated an elongation of 1.8–2.2 % [35] (see Fig. S2 and Table I of the SM [53]). From this comparison, we conclude that the front propagation takes place in the *a*-*b* plane where the most important changes in lattice parameters are observed at the transition.

As explained in Ref. [35], the front propagation starts from the same corner on cooling and heating processes, and the interface adapts itself to the shape of the single crystal so as to minimize the elastic strain accompanying the spin transition. After image processing, we could derive the temporal evolution of the OD at the probed area represented by blue and red squares in Figs. 1(c) and 1(e) during the front propagation. Figure 1(d) illustrates the temporal evolution of the green OD for crystal **1a** on the cooling along the HS to LS transition. The corresponding red and blue ODs for the cooling and heating processes, showing a signal of lower quality compared to the green OD, are represented in Fig. S3 of the SM [53]. First, when the interface crosses the probed area (blue square) at time $t \simeq 15$ s (point P), the OD peaks as a result of the diffusion of light by the interface. The light scattering by the HS/LS interface is also at the origin of the dark character of the front interface. Far from this peak region, the ODs of the HS and LS states are stationary ($\mathrm{OD}_{\mathrm{HS}} = 0.06$, $\mathrm{OD}_{\mathrm{LS}} = 0.95$) with significantly different values, due to the thermochromic character of the present phase transition. On the other hand, we notice the existence of precursor effects on the OD signal long before the interface reaches the probed area, which corresponds to point P. These precursor effects manifest through the emergence of a sudden decrease of the OD in the HS region around $t \simeq 8$ s (point A and the green dashed circle), i.e., almost 5 s before the front arrival. This corresponds to a detection distance $AP \simeq 30\ \mu$m, which is significantly higher than that of the probe (2 μm) and the thickness of the front (less that 1 μm), which is very thin. Figure 1(f) displays the same investigation in the heating regime (at $T \simeq 163$ K). As with cooling, the pic corresponds to the time at which the interface crosses the probed area noted by point P around $t \simeq 16$ s. Contrary to the previous situation, the long-range volume change impacts the OD signal after the transition of the probed region from the LS to the HS state. Indeed, one can easily observe in Fig. 1(f) an after-effect phenomenon, since the OD signal decreases after the interface crossed the point P (green dashed circle) before reaching the stable value of a full HS state at point A around $t \simeq 19$ s. So in this situation, the interface passage leaves a trace on the OD of the probed area, which is now in the HS state.

From these observations of cooling and heating regimes, we can conclude that precursor phenomena on the OD signal are detected only when the probed point is in the HS state, indicating that the HS phase experiences a tensile stress (the lattice parameter is expanded more than its equilibrium value in the HS state) as a feedback or counter-reaction to the pressure forces exerted by the LS transformed region. This behavior is interpreted as proof of the long-range elastic stresses that propagate with the HS-LS interface as a result of the global volume contraction during the spin transition.

The same procedure is now applied to crystal **1b** of Fig. 2 in order to explore the possible differences from one single crystal to another of the same compound. Figure 2(a) reports the temperature dependence of the HS fraction n_{HS}, resulting

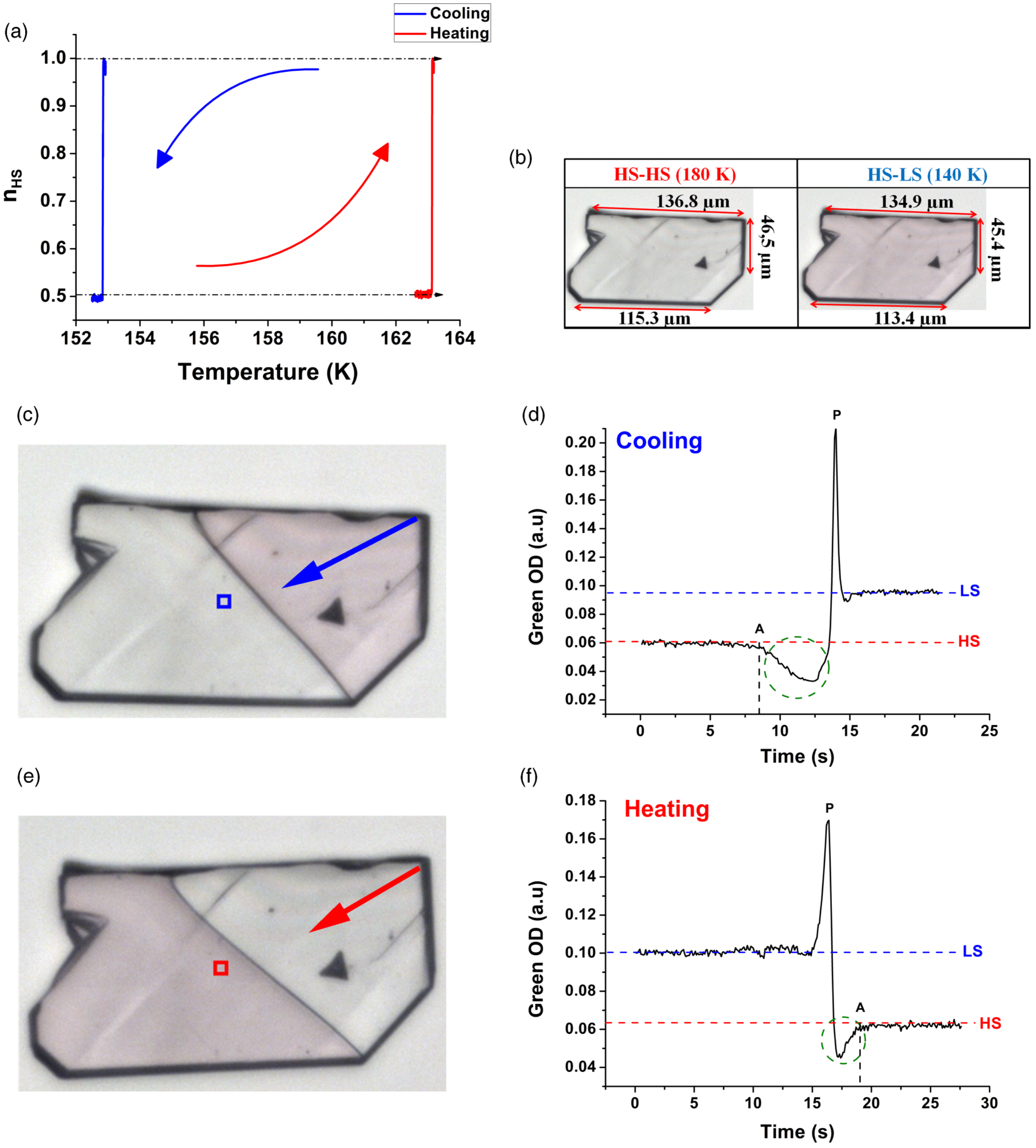

FIG. 1. (a) Temperature dependence of the HS fraction (n_{HS}), derived for OM data and adapted from Ref. [35], showing the occurrence of a thermal hysteresis loop, with alternating temperatures $T \simeq 153$ K and $T \simeq 163$ K for cooling and heating. The temperature sweep rate was 0.2 K min^{-1}. (b) OM images of a rectangular-shaped single crystal of compound (**1a**) including its dimensions in the high- and low-temperature phases [35]. Panels (c) and (e) display selected crystal snapshots with HS/LS front interface along the cooling (153 K) and heating processes (163 K), respectively. The blue and red arrows indicate the propagation direction of the interface. The blue and red squares correspond to the selected areas where the OD is probed. Panels (d) and (f) are the time dependence of the local green OD, measured in the previous defined probed area of the single crystal. Point P appearing in the curves relates to the time at which the interface crosses the probed square region. Point A and the dashed green circle highlight the region where the probe feels the strain field [35].

from the OM investigations of the single crystal **1b**. The latter is derived from the thermal dependence of the green OD using Eq. (2), which showed the best noise-to-signal ratio, compared with the responses of the blue and red OD, as depicted in Fig. S4 of the SM [53]. Thus, Fig. 2(a) shows the occurrence of a first-order thermoinduced spin transition with a hysteresis width of 12 K, and transition temperatures $T \simeq 150$ K and $T \simeq 162$ K for the cooling and heating regimes, respectively. It is worth noting that the thermal evolutions of the HS fractions of Figs. 1(a) and 2(a) are different, although the two

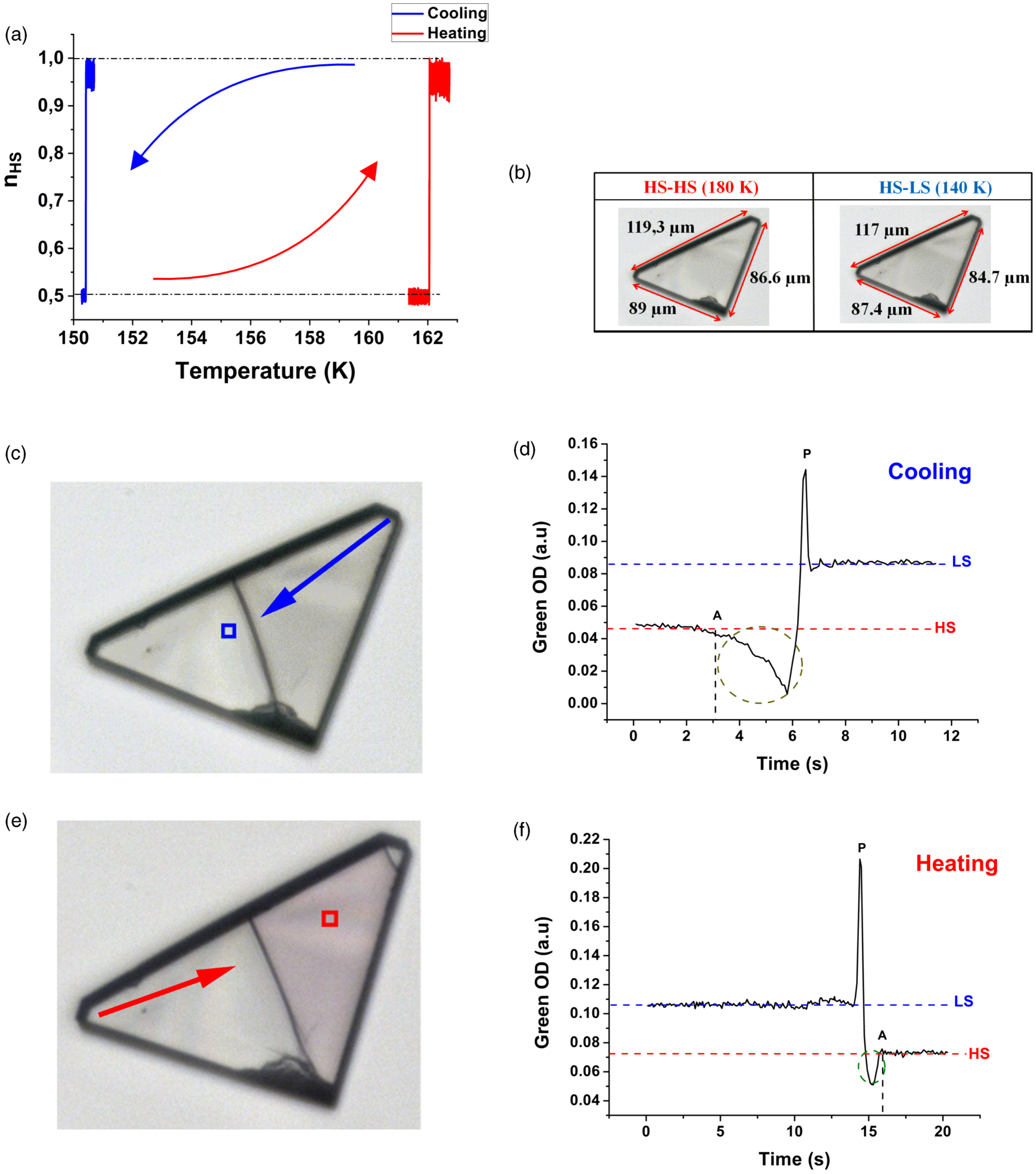

FIG. 2. (a) Temperature dependence of the HS fraction (n_{HS}), derived for OM data and adapted from Ref. [35], showing the occurrence of a thermal hysteresis loop, with alternating temperatures $T \simeq 150$ K and $T \simeq 162$ K for cooling and heating. The temperature sweep rate was 0.2 K min^{-1}. (b) OM images of a triangular-shaped single crystal of compound (**1b**) including its dimensions in the high- and low-temperature phases [35]. Panels (c) and (e) display the crystal snapshots with HS/LS front interface along the cooling (150 K) and heating (162 K) regimes, respectively. The blue and red arrows indicate the propagation direction of the front. The blue and red squares correspond to the selected surface where the OD is measured. Panels (d) and (f) are the time dependence of the local green OD as a function of time, measured in the previous defined probed area of the single crystal. Point *P* appearing in the curves relates to the time at which the interface crosses the probed square. Point *A* and the dashed green circle highlight the region where the probe feels the strain field [35].

crystals belong to the same compound and the same batch. This may be attributed (i) to the effect of the global shape of the crystal, which influences the dynamics of the front motion (due to the long-range interactions acting inside the crystal), or (ii) to the possible difference in thicknesses of the two single crystals, which can affect the quantitative value of the OD. Similarly to single crystal **1a**, Fig. 2(b) summarizes the different lengths of the studied single crystal in both HS and LS states. The macroscopic relative size variations of the single crystal are estimated to be 1.8–2.2 %, in excellent agreement with x-ray data results that indicated an elongation of 1.8–2.2 % [35] (see Fig. S5 and Table II of the SM [53]). From this comparison, we conclude that the front propagation takes place in the *a*-*b* plane where the most important changes in lattice parameters are observed at the transition.

Figure 2(d) displays the temporal evolution of green OD response at the front passage in the vicinity of the probed area represented in the snapshot of Fig. 2(c) along the cooling branch of the thermal hysteresis. Similar to compound **1a**, the red and blue OD responses (reported in Figs. S6a and S6b of the SM [53]) displayed slightly more fluctuations compared to that of the green OD. We observe a similar global behavior to that for single crystal **1a** [Fig. 1(d)] with a peak of the OD at $t \simeq 7$ s, corresponding to the time at which the interface crosses the probed region (point P). Far from point P, we identify two stable lines corresponding to the stable HS and LS states, where OD values are, respectively, $\mathrm{OD}_{\mathrm{HS}} = 0.05$ and $\mathrm{OD}_{\mathrm{LS}} = 0.9$.

On the other hand, we can see also the decrease in the OD signal starting from point A at $t \simeq 3$ s (dashed green circle). Figure 2(f) displays the OD of the probed area of Fig. 2(e) upon heating where the HS propagates into the LS at $T \simeq 162$ K. The interface crosses the probed region at point P corresponding to time $t \simeq 14$ s. We identify the decrease of the OD signal from point P to point A, highlighted on the graph by the dashed green circle, comparing to the stable value of an HS state corresponding to $\mathrm{OD}_{\mathrm{HS}} = 0.07$ starting at point A at $t \simeq 16$ s. The same phenomenon of long-range effects is identified by the decrease of the OD value in the HS part, which is affected by the strain generated by the volume change during the propagation of the HS/LS interface.

For more consistency, we extend the OM investigations to the compound (**2**) of Ref. [36], for which the single crystals undergo a first-order spin transition as displayed in Fig. 2. Similar to compound (**1**), the corresponding temperature dependence of the HS fraction is derived from the thermal dependence of the green OD using Eq. (2), which showed the best noise-to-signal ratio compared with the responses of the blue and red OD, which are presented in Fig. S7 of the SM [53]. Figure 3(a) shows a thermal hysteresis of 10 K width with alternating transition temperatures of $T \simeq$ 143 K and $T \simeq 153$ K for the cooling and heating processes, respectively. Here also the single crystal manifests a volume change during the spin transition as confirmed in the snapshots of Fig. 3(b), where the different crystal sizes in HS and LS states are presented. Similar to the previous cases of Figs. 1 and 2, the relative variation of the crystal dimensions between the HS and LS states, derived from OM, lead to the values 1–2.2 %, which are in good agreement with x-ray measurements that indicated an elongation of 1.8–2.2 % [36] (see Fig. S8 and Table III of the SM [53]). From this comparison, it is concluded that the front propagation takes place in the *a*-*b* plane.

The same experimental procedure of investigations of the long-range aspect of the spin transition is applied to compound **2**. Figures 3(d) and 3(f) summarize the temporal evolution of the green OD in the vicinity of the probe along the respective cooling and heating processes of the thermal hysteresis. The OD responses of the other red and blue pixels are represented in Figs. S9a and S9b of the SM [53], showing a similar behavior to that of the green OD. The selected probed surface is represented in Figs. 3(c) and 3(e) by blue and red squares for cooling and heating regimes, respectively. Figure 3(d) displays the cooling regime where the LS state propagates into the HS state; the passage of the front interface is identified by the pic (point P) taking place at $t \simeq 80$ s. Here also, a remarkable change of the OD takes place, well before the arrival of the front interface, from point A at $t \simeq 57$ s, highlighted by the dashed green circle on the graph. Far from that region, the OD signal takes stationary values of HS and LS states ($\mathrm{OD}_{\mathrm{HS}} = 0.17$ and $\mathrm{OD}_{\mathrm{LS}} = 0.2$). Figure 3(f) displays the heating process, the green OD signal peaks in the vicinity of the probed region, and it does not show any precursor phenomena. However, a clear after effect of the front passage is recorded in the HS region. The interface crosses the probed area at point P at $t \simeq 75$ s, the change of the OD signal due to the long-range effect is highlighted by the dashed green circle, and from point A at $t \simeq 87$ s the system reaches the OD value of the HS state ($\mathrm{OD}_{\mathrm{HS}} =$ 0.17).

The last studied example is that of compound (**3**) [34,37,50,52], for which we selected a high-quality single crystal (see Fig. 4). The thermal dependence of the HS fraction is derived from the thermal dependence of the green OD using Eq. (2), which showed the best noise-to-signal ratio compared with the responses of the blue and red OD, depicted in Figs. S10a and S10c of the SM [53]. Figure 4(a) indicates that the studied single crystal exhibits a sharp first-order spin transition accompanied by a thermal hysteresis loop of 8 K width. The alternating transition temperatures of the thermal hysteresis upon cooling and heating are $T \simeq 104$ K and $T \simeq 112$ K, respectively. The volume change at the spin transition is also significant, as indicated in Fig. 4(b), where the main crystal's length expands by $\simeq 2.2\%$ upon the LS to HS transition. This value is also in good agreement with structural data of the literature, which reported an elongation of $\simeq 2.6\%$ [34] (see Fig. S11 and Table IV of the SM [53]). For this compound, the x-ray diffraction also proved that the crystal length corresponds to the *b* direction of the lattice parameter, which showed the most significant change at the thermal transition. Following the previous procedures, we present in Figs. 4(d) and 4(f) the temporal evolution of the red OD, probed on a small area of the crystal, represented in Figs. 4(c) and 4(e) upon cooling and heating, respectively. The other responses of the green and blue OD are represented in Fig. S12 [53], showing qualitatively the same behavior as the chosen red OD. Similar trends are found for the present crystal, since the front propagation influences the OD of the probed region before its arrival [Fig. 4(d)] upon cooling and after its passage [Fig. 4(f)] upon heating. In both

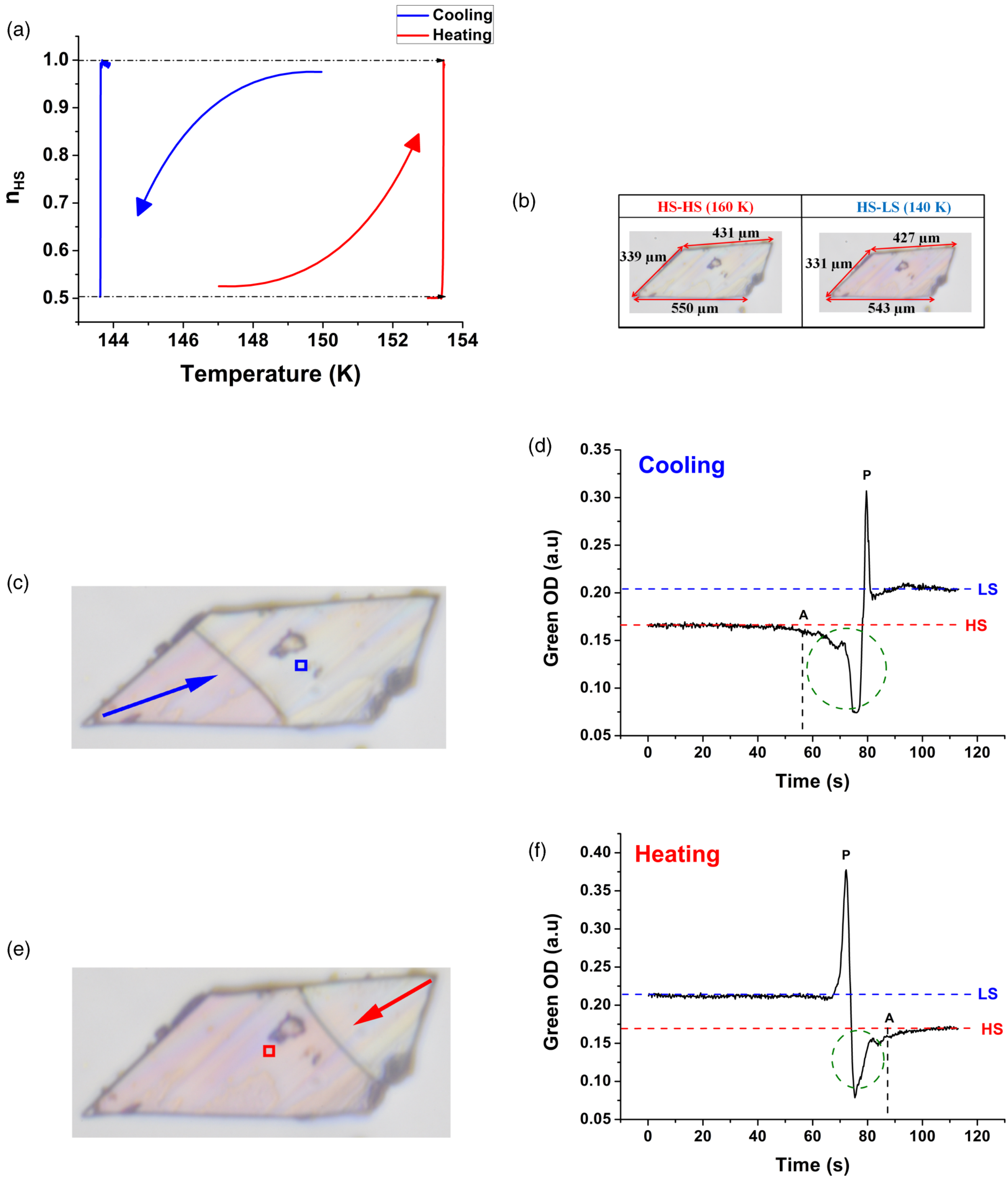

FIG. 3. (a) Temperature dependence of the HS fraction (n_{HS}), derived for OM data and adapted from Ref. [36], showing the occurrence of a thermal hysteresis loop with alternating temperatures $T \simeq 143$ K and $T \simeq 153$ K for cooling and heating, respectively. The temperature sweep rate was 0.5 K min^{-1}. (b) OM images of the single crystal of compound (**2**) including its dimensions in the high- and low-temperature phases [36]. Panels (c) and (e) display the crystal snapshots with HS/LS front interface along the cooling and heating, respectively. The blue and red arrows indicate the propagation direction of the front. The blue and red squares correspond to the selected areas where the OD is probed. Panels (d) and (f) are the time dependence of the local green OD, measured in the previous defined probed area of the single crystal. Point *P* appearing in the curves relates to the time at which the propagating interface crosses the square. Point *A* and the dashed green circle highlight the region where the probe feels the strain field [36].

situations, the probed area reacts as a precursor or as an after effect only when it is in the HS phase, in accordance with the response of the single crystals (**1a**), (**1b**), and (**2**), although the amplitude of the OD changes of the probe seems to be much more reduced in the present case. Again, one can conclude that the front propagation deploys long-range changes that can be captured by the change of OD in the HS phase only.

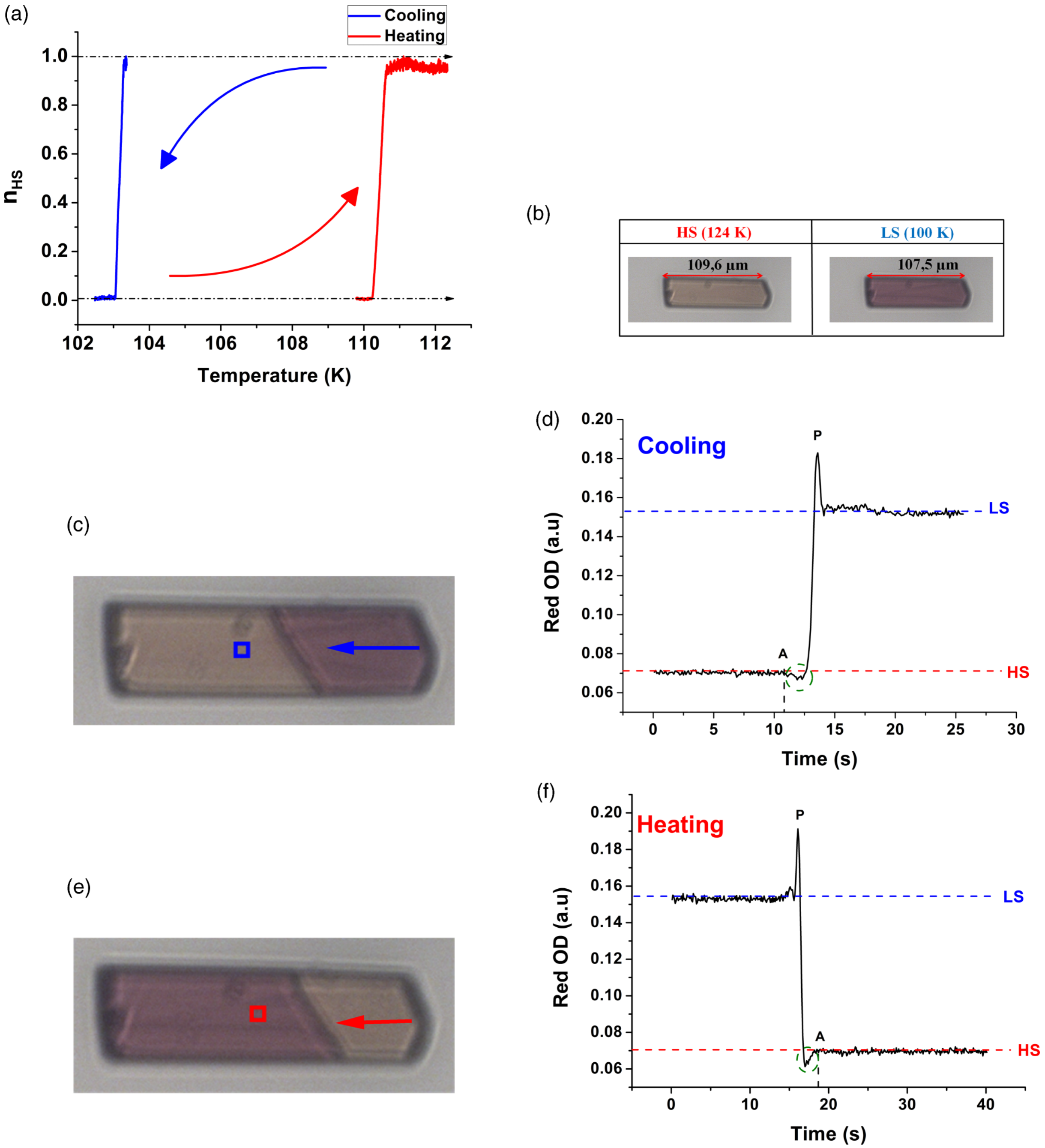

FIG. 4. (a) Temperature dependence of the HS fraction (n_{HS}), derived for OM data and adapted from Ref. [37], showing the occurrence of a thermal hysteresis loop, with alternating temperatures $T \simeq 104$ K and $T \simeq 112$ K for cooling and heating. The temperature sweep rate is 0.2 K min^{-1}. (b) OM images of the single crystal of compound (**3**) including its dimensions in the high- and low-temperature phases [37]. Panels (c) and (e) display the crystal snapshots with the presence of a HS/LS front interface along the lower (~104 K) and the upper (~112 K) transition temperatures, respectively. The blue and red arrows indicate the propagation direction of the front. The blue and red squares correspond to the selected areas where the OD is probed. Panels (d) and (f) are the time dependence of the red OD, measured in the previous defined probed area of the single crystal. Point P appearing in the curves relates to the time at which the propagating interface crosses the square. Point A and the dashed green circle highlight the region where the probe feels the strain field.

III. THEORETICAL DESCRIPTION

In the present work, we investigate the elastic properties of a discrete two-dimensional rectangular lattice. We consider an electroelastic model (some of the thermodynamic properties of which we have already considered in recent works [34,43,48–50]) to mimic the SCO transition. The considered rectangular system is placed with respect to the square symmetry, and each node of the lattice has four nearest neighbors and four next-nearest neighbors. Every node is considered as SCO molecule, and it can be in the HS or LS state described by two fictitious spins $S_i = +1$ and -1 for HS and LS, respectively. The distance and the interactions between the molecules depend on their spin states. In fact, the interactions between the nearest and next-nearest neighbors may be considered through springs whose stiffness depends on the instantaneous distance. The total Hamiltonian of the system accounting for electronic and elastic contributions is written as

$$H=\sum_i \frac{(\Delta - k_B T \ln g)S_i}{2} + \sum_{i,j} A(S_i,S_j)[r_{ij}-R_0(S_i,S_j)]^2 + \sum_{i,k} B(S_i,S_k)[r_{ik}-R_0(S_i,S_k)]^2. \tag{3}$$

The first term of Eq. (3) is the energy gap separating the LS and HS states of an isolated molecule. It contains the energy contribution, Δ, arising from the difference of ligand field energies in the HS and LS states, and the entropic contribution $k_B \ln g$ resulting from the electro-vibrational degeneracy ratio, g, between the HS and LS states. The second and third terms of Hamiltonian (3) account for elastic interactions between nearest neighbors (nn) and next-nearest neighbors (nnn) of SCO units. $R_0(S_i, S_j)$ are the equilibrium bond lengths between the nodes i and j depending on the bond type: $R_0(+1,+1) = R_0^{HH}$, $R_0(+1,-1) = R_0(-1,+1) = R_0^{HL}$, and $R_0(-1,-1) = R_0^{LL}$, where R_0^{HH}, R_0^{HL}, and R_0^{LL} are the respective equilibrium distances between HS-HS, HS-LS, and LS-LS sites. Similarly to the equilibrium distances, we choose nn (nnn) elastic constants $A(S_i, S_j)$ $[B(S_i, S_k)]$ depending on the spin states, such as $A(+1,+1) = A^{HH}$ $[B(+1,+1) = B^{HH}]$, $A(+1,-1) = A(-1,+1) = A^{HL}$ $[B(+1,-1) = B(-1,+1) = B^{HL}]$, and $A(-1,-1) = A^{LL}$ $[B(-1,-1) = B^{LL}]$, where A^{HH} (B^{HH}), A^{HL} (B^{HL}), and A^{LL} (B^{LL}) are the nn (nnn) elastic constants between HS-HS, HS-LS, and LS-LS sites. It is straightforward to demonstrate that there is a general expression linking the equilibrium positions $[R_0(S_i, S_j)]$ and elastic constants $[A(S_i, S_j), B(S_i, S_j)]$ to the spin states S_i, S_j:

$$X(S_i, S_j) = X^{HL} + \delta_X \frac{S_i + S_j}{4}, \tag{4}$$

where $\delta_X = X^{HH} - X^{LL}$ and $X^{HL} = \frac{X^{HH}+X^{LL}}{2}$. Here $X(S_i, S_j)$ can be either $R_0(S_i, S_j)$, $A(S_i, S_j)$, or $B(S_i, S_j)$.

The following parameter values are used in the simulations: $\Delta = 450$ K for the ligand field energy; $g = 150$ for the degeneracy ratio; and $R_0^{HH} = 1.2$ nm, $R_0^{LL} = 1.0$ nm, and $R_0^{HL} = 1.1$ nm for the equilibrium nn distances (lattice parameters). The nnn equilibrium distances are simply taken to be equal to those of the nn multiplied by $\sqrt{2}$, due to the adopted 2D square lattice symmetry. The elastic constants are $A^{HH} = 10^4$ K nm^{-2}, $A^{LL} = 2 \times 10^5$ K nm^{-2}, $A^{HL} = \frac{A^{HH}+A^{LL}}{2} = 1.05 \times 10^5$ K nm^{-2}, $B^{HH} = 0.3 \times A^{HH}$, $B^{LL} = A^{LL}$, and $B^{HL} = \frac{B^{HH}+B^{LL}}{2}$.

The MC procedure is performed on spin variables and atomic positions as follows: we choose an atom randomly and flip its spin state using the usual MC METROPOLIS algorithm. In any case (spin flip accepted or rejected), we visit randomly and sequentially all of the lattice sites and attempt to move each site by some quantity $\delta u << R_0$ in a randomly chosen direction. If the usual MC METROPOLIS algorithm permits the new position, then we update the position of the atom; if it is forbidden, the atom is left in its original position. Then, we choose randomly a new site for which we perform the same procedure. The algorithm of relaxation of all lattice positions is repeated 10 times for each spin flip to reach the stable mechanical state. Next, we update each of the $N_x \times N_y$ spins, using the same procedure. Now, we examine the relaxation of metastable HS states at low temperatures for a rectangular lattice $N_x \times N_y = 70 \times 20$. Such a metastable state may be obtained by photoexcitation through the light-induced-excited-spin-state trapping (LIESST effect) [54–57] or by rapid quenching of the high-temperature HS state.

The goal of this work is to understand the effect of long-range interactions on a system with a very rigid LS state and a soft HS state. The calculations are performed at a temperature $T = 10$ K so as to avoid the thermal fluctuations that complicate the analysis of the data. In so doing, we initially prepare all of the sites in the HS state by setting all spin values at $S_i = +1$ and all nn distances at $r_{ij} = 1.2$ nm. We then change the spin states of the lattice line by line going from $i = 1$ to 70 $(S_i = -1)$, and at every change we perform MC simulations on the lattice positions so as to reach the mechanical equilibrium.

In so doing, we obtain 70 configurations showing the front propagation. Figure 5(a) displays an example of a relaxed HS/LS configuration in which the HS/LS interface is located at $N_x = 35$. There, we see evidence of a clear volume contraction in the LS lattice due to the presence of an elastic interface. The corresponding energy relaxation presented in Fig. 5(b) shows that the system reaches its mechanical equilibrium after $\simeq 2500$ MC steps (MCS) where all forces vanish in the system while internal pressure still exists. Indeed, internal local pressure on site i, which corresponds to the gradient of local elastic energy, can be obtained from Hamiltonian (1) through the following expression:

$$P_i = -\sum_j A_{ij}[r_{ij} - R(S_i, S_j)] - \sum_k B_{ik}[r_{ik} - \sqrt{2}R(S_i, S_k)]. \tag{5}$$

The spatial distribution of the internal pressure of the electroelastic configuration [Fig. 5(a)] is represented in Fig. 5(c), which indicates that the pressure field is stored not only in the front part, but also far away, which serves as proof of the effect of long-range interactions in the system.

To mimic the experimental analysis, we calculate the average distances $\langle d \rangle$ between two successive sites along the x-direction inside the probed square situated at coordinates (34,35) in all configurations. We plot in Figs. 6(a) and 6(b) the average distance, $\langle d \rangle$, as a function of time for HS to LS and LS to HS transformations, respectively. In Fig. 6(a) [6(b)], the system is initially prepared in the HS (LS) state, which leads to $\langle d \rangle \simeq R_0^{HH}$ (R_0^{LL}). Then the LS (HS) domain propagates inside the lattice causing its contraction (expansion). In Fig. 6(a), the LS state is propagating and pulling the system so as to decrease the lattice parameter. Due to the strong rigidity of the LS state and the soft character of the HS state, the average lattice parameter of the HS phase at the interface increases more than its equilibrium value, R_0^{HH}. In addition, this change started before reaching the probed square, in agreement with experimental observations.

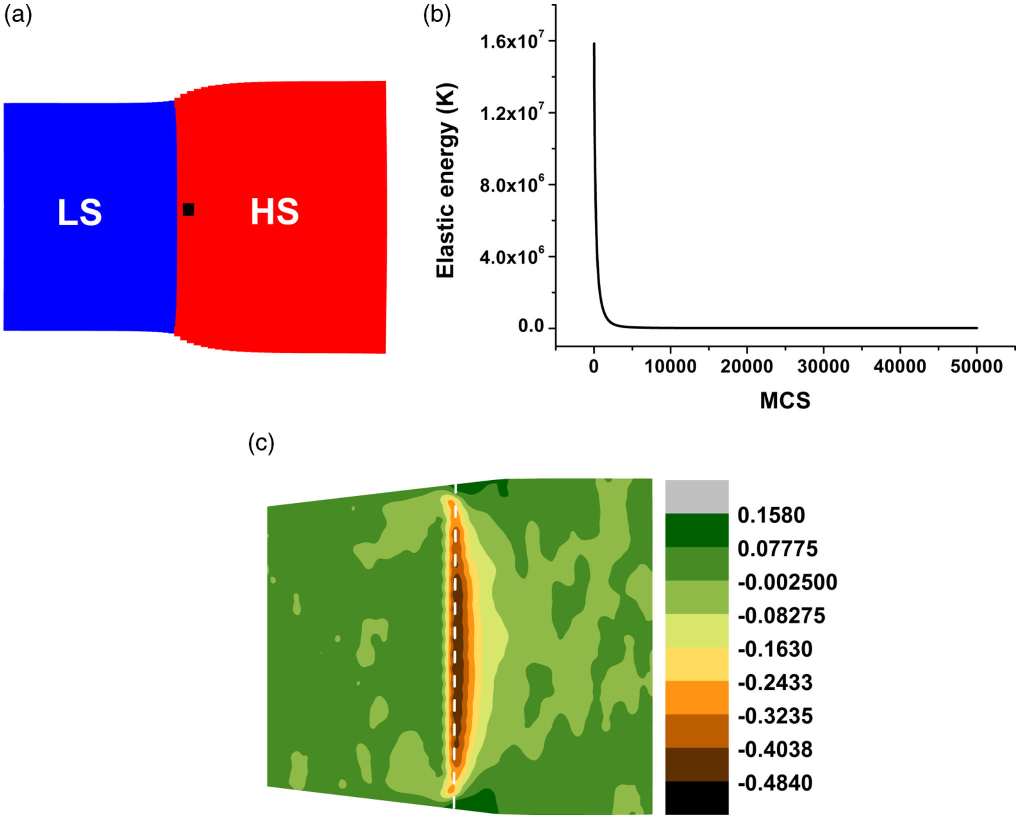

FIG. 5. (a) Snapshot of the relaxed lattice configuration with a fixed front interface position at $i = N_x/2$. The black square indicates the probed area. Blue and red regions represent the LS and HS phases, respectively. (b) Time dependence (MCS) of the elastic energy during the mechanical relaxation at fixed electronic configuration. The initial configuration is made of half spins -1 and $+1$ while all distances are set equal to those of the HS state. (c) Spatial distribution of the internal pressure field inside the lattice, corresponding to panel (a). The HS-LS interface is represented by the dashed white line. The lattice size is $N_x \times N_y = 70 \times 20$. The other parameter values are given in the text.

After crossing the probe, the system switches in the LS state and the average equilibrium distance becomes equal to R_0^{LL}. In Fig. 6(b), the HS phase propagates inside the LS phase. The rigidity of the LS phase prevents any elastic precursor effects, while they clearly appear in the HS state after the switching of the probe.

The theoretical OD equation is

$$\mathrm{OD} = \frac{\alpha}{\langle d\rangle} + \beta \frac{\partial \langle d\rangle}{\partial t}. \tag{6}$$

The first term is related to the dependence of the OD as the mass density of the material, taking into account the change of the OD with the volume so as to have OD(LS) > OD(HS).

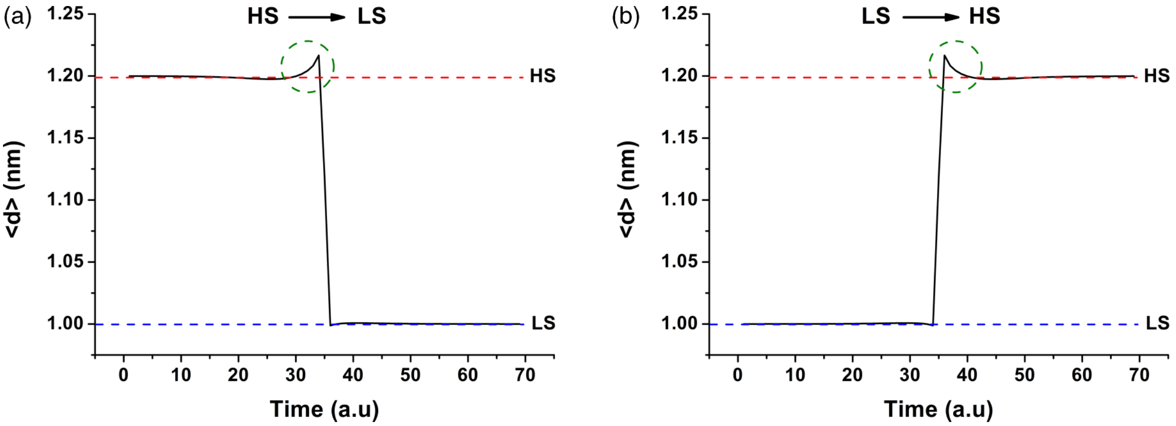

FIG. 6. Time dependence of the local average distance $\langle d\rangle$ measured in the probed area, represented by the black square of Fig. 5(a), during the interface propagation along the (a) HS to LS and (b) LS to HS phase transitions. The simulations are performed at 10 K and the lattice size is $N_x \times N_y = 70 \times 20$.

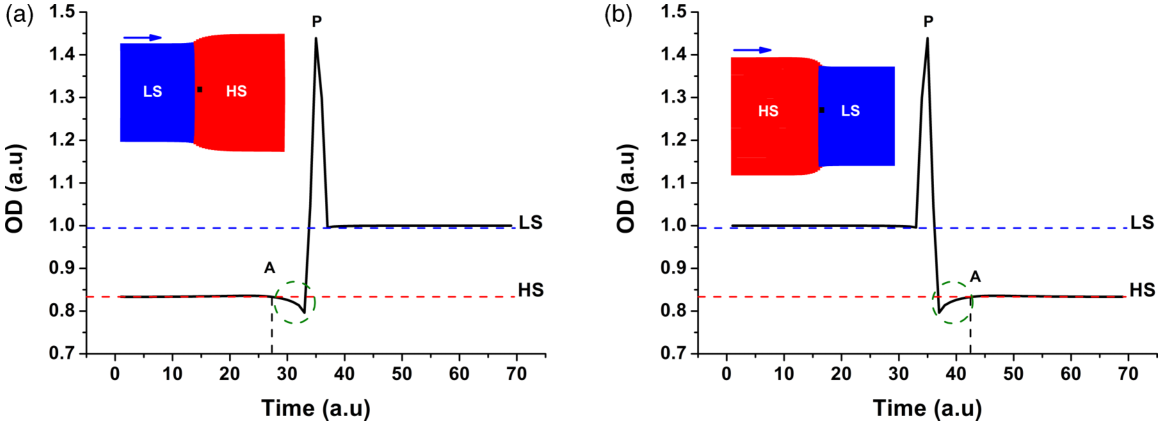

FIG. 7. Time dependence of the theoretical OD evaluated at the black square probed area (see the insets) along the (a) HS to LS and (b) LS to HS phase transitions. The curves are calculated using Eq. (6) and the average local distance $\langle d \rangle$ of Fig. 6. A very good qualitative agreement with the experimental results of compounds **1a**, **1b**, **2**, and **3**. The lattice size is $N_x \times N_y = 70 \times 20$.

The second contribution accounts for the change of the OD at the HS-LS interface as a result of light scattering, which causes the weakening of the transmitted light intensity. Within Eq. (6), we analyzed the theoretical results of Fig. 6, which led to the time dependence OD(t) of Fig. 7. The latter is found to be in fair agreement with the results of compounds **1a**, **1b**, **2**, and **3**, which also showed precursor phenomena in the HS state, due to long-range effects as explained in the text. The chosen α and β values are 1 and 5, respectively.

IV. CONCLUSION

We have presented spatiotemporal OM studies on the propagation of the HS/LS interface proving the existence of long-range effects over the course of the spin transition phenomenon. The analysis are performed on the following set of SCO single crystals, [{Fe(NCSe)(py)$_2$}$_2$(m-bpypz)], [{Fe(2-pytrz)$_2$[Pt(CN)$_4$]}] · 3H$_2$O, and [{Fe(2-pytrz)$_2$[Pd(CN)$_4$]}] · 3H$_2$O, that show first-order phase transitions accompanied with thermal hysteresis. The present spin transitions between LS to HS are accompanied by a volume change at the macroscopic scale, originating from local volume changes, which deploy over the whole crystal. It is then expected that the propagation of the HS/LS interface will be preceded or followed by the propagation of a stress field, which will affect the OD (and the refractive index) of the material, well before or after the position of the HS/LS interface. Following these ideas, we tracked the time evolution of the OD in a local region of the material, initially situated far from the HS/LS interface, and we monitored its changes over the course of the spin transition. This experiment is performed along the heating and cooling regimes of the thermal hysteresis of the three studied single crystals, mentioned above. We found in all single crystals that along the cooling branch (HS to LS transition), the local OD starts to change long before (after) the HS/LS interface reaches (crosses) the probed HS area. The fact that this phenomenon appears more pronounced when the probed region is HS phase is certainly due to the significant difference of rigidities between the HS and LS states. The fact that the HS state is softer reveals the existence of precursor phenomena (in the HS to LS transformation) preceding the spin transition at a given point, which manifest themselves through a change in the OD well before the arrival of the front interface. On the other hand, the study of the heating branches (LS to HS transition) does not reveal any precursor change of the OD at a LS region ahead of the interface. In contrast, in all studied samples, an after effect of front passage is observed through a sudden decrease of the OD signal of the HS phase after the front passage. We attribute these effects to the long-range elastic character of the interactions that govern the transformation of cooperative SCO materials.

To confirm these explanations, we performed MC simulations on a 2D distortable electroelastic model, taking into account the volume change at the transition, through the dependence of the local bond lengths on the spin states of the linked sites. In addition, the model accounts for the difference in rigidities of HS and LS phases by considering that the elastic constant of the HS state is smaller than that of the LS state. Due to the volume change at the transition, long-range elastic interactions are generated in this model. In a similar manner to that for the experimental part, we tracked the change of local bond lengths in a fixed region of the lattice during the front propagation. The time dependence of the average local bond lengths, which are connected to the OD of the material, of the probed area showed a change long before the front interface was reached, in good agreement with the experimental data.

ACKNOWLEDGMENTS

The authors warmly thank S. Kaizaki and S. Triki for providing very high quality single crystals, and Y. Singh for reading the manuscript. This work was supported by the CNRS and the Université de Versailles St-Quentin member of the Université Paris–Saclay, which are gratefully acknowledged. H.F. is indebted to the University of Versailles and the French-Japan international laboratory (LIA IM-LED) for the financial support.

[1] E. Coronado, Molecular magnetism: from chemical design to spin control in molecules, materials and devices, Nat. Rev. Mater. **5**, 87 (2020).

[2] K. Boukheddaden, M. H. Ritti, G. Bouchez, M. Sy, M. M. Dîrtu, M. Parlier, J. Linares, and Y. Garcia, Quantitative contact pressure sensor based on spin crossover mechanism for civil security applications, J. Phys. Chem. C **122**, 7597 (2018).

[3] J. Linares, E. Codjovi, and Y. Garcia, Pressure and temperature spin crossover sensors with optical detection, Sensors **12**, 4479 (2012).

[4] J. Zarembwitch and O. Kahn, Spin-transition molecular systems: Towards information storage and signal processing, New J. Chem. **15**, 181 (1991).

[5] O. Kahn, J. Kröber, and C. Jay, Spin transition molecular materials for displays and data recording, Adv. Mater. **4**, 718 (1992).

[6] Y. Garcia, P. J. van Koningsbruggen, E. Codjovi, R. Lapouyade, O. Kahn, and L. Rabardel, Non-classical feii spin-crossover behavior leading to an unprecedented extremely large apparent thermal hysteresis of 270 k: application for displays, J. Mater. Chem. **7**, 857 (1997).

[7] O. Kahn and C. Jay-Martinez, Spin-transition polymers: From molecular materials toward memory devices, Science **279**, 44 (1998).

[8] P. Gütlich, Spin crossover in iron(ii)-complexes, in *Metal Complexes*, Structure and Bonding Vol. 44 (Springer, Berlin, 1981), Book Sec.2, pp. 83–195.

[9] P. Gütlich and H. Goodwin, Spin crossover—An overarce>, Top. Curr. Chem. 233, 1 (2004).

[10] P. Gütlich, A. Hauser, and H. Spiering, Thermal and optical switching of iron(ii) complexes, Angew. Chem., Int. Ed. Engl. **33**, 2024 (1994).

[11] C. P. Köhler, R. Jakobi, E. Meissner, L. Wiehl, H. Spiering, and P. Gütlich, Nature of the phase transition in spin crossover compounds, J. Phys. Chem. Solids **51**, 239 (1990).

[12] E. König, Nature and dynamics of the spin-state interconversion in metal complexes, in *Complex Chemistry*, Structure and Bonding Vol. 76 (Springer, Berlin, 1991), Book Sec.2, pp. 51–152.

[13] A. Bousseksou, N. Negre, M. Goiran, L. Salmon, J. P. Tuchagues, M. L. Boillot, K. Boukheddaden, and F. Varret, Dynamic triggering of a spin-transition by a pulsed magnetic field, Eur. Phys. J. B **13**, 451 (2000).

[14] A. Hauser, J. Jeftic, H. Romstedt, R. Hinek, and H. Spiering, Cooperative phenomena and light-induced bistability in iron(II) spin-crossover compounds, Coord. Chem. Rev. **190**, 471 (1999).

[15] O. Kahn, *Molecular Magnetism* (Wiley-VCH, New York, 1993), p. 53.

[16] O. Sato, J. Tao, and Y.-Z. Zhang, Control of magnetic properties through external stimuli, Angew. Chem. Int. Ed. **46**, 2152 (2007).

[17] K. Nishi, S. Arata, N. Matsumoto, S. Iijima, Y. Sunatsuki, H. Ishida, and M. Kojima, One-dimensional spin-crossover iron(ii) complexes bridged by intermolecular imidazole-pyridine NH...N hydrogen bonds, $[Fe(HL^{Me})_3]X_2$ ($HL^{Me} =$ (2-methylimidazol-4-yl-methylideneamino-2-ethylpyridine; $X = PF_6, ClO_4, BF_4$), Inorg. Chem. **49**, 1517 (2010).

[18] M. Koike, K. Murakami, T. Fujinami, K. Nishi, N. Matsumoto, and Y. Sunatsuki, Syntheses, three types of hydrogen-bonded assembly structures, and magnetic properties of $[Fe^{III}(Him)_2(hapen)]$Y.solvent (Him=imidazole, hapen=N,N′-bis(2-hydroxyacetophenylidene)ethylenediamine, $Y = BPh_4^-$, $CF_3SO_3^-$, PF_6^-, ClO_4^-, and BF_4^-), Inorg. Chim. Acta **399**, 185 (2013).

[19] M. Nihei, H. Tahira, N. Takahashi, Y. Otake, Y. Yamamura, K. Saito, and H. Oshio, Multiple bistability and tristability with dual spin-state conversions in $[Fe(dpp)_2][Ni(mnt)_2]_2 \cdot MeNo_2$, J. Am. Chem. Soc. **132**, 3553 (2010).

[20] T. Kosone, I. Tomori, C. Kanadani, T. Saito, T. Mochida, and T. Kitazawa, Unprecedented three-step spin-crossover transition in new 2-dimensional coordination polymer $Fe^{I}I(4-\text{methylpyridine})_2[Au^{I}(CN)_2]_2$, Dalton Trans. **39**, 1719 (2010).

[21] D. Chiruta, C.-M. Jureschi, J. Linares, P. R. Dahoo, Y. Garcia, and A. Rotaru, On the origin of multi-step spin transition behavior in 1d nanoparticles, Eur. Phys. J. B **88**, 233 (2015).

[22] T. Kambara, The effect of iron concentration on the high-spin low-spin transitions in iron compounds., J. Phys. Soc. Jpn. **49**, 1806 (1980).

[23] N. Sasaki, Theory of cooperative high-spin low-spin transitions in iron (III) compounds induced by the molecular distortions, J. Chem. Phys. **74**, 3472 (1981).

[24] S. W. Biernacki and B. Clerjaud, Thermally driven low-spin/high-spin phase transitions in solids, Phys. Rev. B **72**, 024406 (2005).

[25] G. D'Avino, A. Painelli, and K. Boukheddaden, Vibronic model for spin crossover complexes, Phys. Rev. B **84**, 104119 (2011).

[26] S. Pillet, J. Hubsch, and C. Lecomte, Single crystal diffraction analysis of the thermal spin conversion in $[Fe(btr)_2(NCS)_2](H_2O)$: Evidence for spin-like domain formation, Eur. Phys. J. B **38**, 541 (2004).

[27] S. Gawali-Salunke, F. Varret, I. Maurin, C. Enachescu, M. Malarova, K. Boukheddaden, E. Codjovi, H. Tokoro, S. Ohkoshi, and K. Hashimoto, Magnetic and mössbauer investigation of the photomagnetic prussian blue analog $Na_{0.32}Co[Fe(CN)_6]_{0.74} \cdot 3.4H_2O$: Cooperative relaxation of the thermally quenched state, J. Phys. Chem. B **109**, 8251 (2005).

[28] F. Varret, C. Chong, A. Goujon, and K. Boukheddaden, Light-induced phase separation (LIPS) in $[Fe(ptz)_6](BF_4)_2$ spin-crossover single crystals: Experimental data revisited through optical microscope investigation, J. Phys.: Conf. Ser. **148**, 012036 (2009).

[29] C. Chong, A. Slimani, F. Varret, K. Boukheddaden, E. Collet, J. C. Ameline, R. Bronisz, and A. Hauser, The kinetics features of a thermal spin transition characterized by optical microscopy on the example of $[Fe(bbtr)_3](ClO_4)_2$ single crystals: Size effect and mechanical instability, Chem. Phys. Lett. **504**, 29 (2011).

[30] A. Goujon, F. Varret, K. Boukheddaden, C. Chong, J. Jeftic, Y. Garcia, A. D. Naik, J. C. Ameline, and E. Collet, An optical microscope study of photo-switching and relaxation in single crystals of the spin transition solid $[Fe(ptz)_6](BF_4)_2$, with image processing, Inorg. Chim. Acta **361**, 4055 (2008).

[31] C. Chong, H. Mishra, K. Boukheddaden, S. Denise, G. Bouchez, E. Collet, J.-C. Ameline, A. D. Naik, Y. Garcia, and F. Varret, Electronic and structural aspects of spin transitions observed by optical microscopy. the case of $[Fe(ptz)_6](BF_4)_2$, J. Phys. Chem. B **114**, 1975 (2010).

[32] A. Slimani, F. Varret, K. Boukheddaden, C. Chong, H. Mishra, J. Haasnoot, and S. Pillet, Visualization and quantitative analysis of spatiotemporal behavior in a first-order thermal spin transition: A stress-driven multiscale process, Phys. Rev. B **84**, 094442 (2011).

[33] F. Varret, A. Slimani, K. Boukheddaden, C. Chong, H. Mishra, E. Collet, J. Haasnoot, and S. Pillet, The propagation of the thermal spin transition of $[Fe(btr)_2(NCS)_2](H_2O)$ single crystals, observed by optical microscopy, New J. Chem. **35**, 2333 (2011).

[34] M. Sy, F. Varret, K. Boukheddaden, G. Bouchez, J. Marrot, S. Kawata, and S. Kaizaki, Structure-driven orientation of the high-spin-low-spin interface in a spin-crossover single crystal, Angewandte Chemie **126**, 7669 (2014).

[35] H. Fourati, E. Milin, A. Slimani, G. Chastanet, Y. Abid, S. Triki, and K. Boukheddaden, Interplay between a crystal's shape and spatiotemporal dynamics in a spin transition material, Phys. Chem. Chem. Phys. **20**, 10142 (2018).

[36] H. Fourati, G. Bouchez, M. Paez-Espejo, S. Triki, and K. Boukheddaden, Spatio-temporal investigations of the incomplete spin transition in a single crystal of $[Fe(2-pytrz)_2Pt(CN)_4]\cdot 3H_2O$: Experiment and theory, Crystals **9**, 46 (2019).

[37] M. Sy, R. Traiche, H. Fourati, Y. Singh, F. Varret, and K. Boukheddaden, Spatiotemporal investigations on light-driven high-spin-low-spin interface dynamics in the thermal hysteresis region of a spin-crossover single crystal, J. Phys. Chem. C **122**, 20952 (2018).

[38] F. Varret, C. Chong, A. Slimani, D. Garrot, Y. Garcia, and A. D. Naik, Real-time observation of spin-transitions by optical microscopy, in *Spin-Crossover Materials* (John Wiley & Sons Ltd, UK, 2013), pp. 425–441.

[39] S. Bedoui, G. Molnár, S. Bonnet, C. Quintero, H. J. Shepherd, W. Nicolazzi, L. Salmon, and A. Bousseksou, Raman spectroscopic and optical imaging of high spin/low spin domains in a spin crossover complex, Chem. Phys. Lett. **499**, 94 (2010).

[40] M. Castro, O. Roubeau, L. Piñeiro-Lápez, J. A. Real, and J. A. Rodríguez-Velamazán, Pulsed-laser switching in the bistability domain of a cooperative spin crossover compound: A critical study through calorimetry, J. Phys. Chem. C **119**, 17334 (2015).

[41] M. Nishino, C. Enachescu, S. Miyashita, K. Boukheddaden, and F. Varret, Intrinsic effects of the boundary condition on switching processes in effective long-range interactions originating from local structural change, Phys. Rev. B **82**, 020409 (2010).

[42] M. Nishino, T. Nakada, C. Enachescu, K. Boukheddaden, and S. Miyashita, Crossover of the roughness exponent for interface growth in systems with long-range interactions due to lattice distortion, Phys. Rev. B **88**, 094303 (2013).

[43] M. Nishino, C. Enachescu, S. Miyashita, P. A. Rikvold, K. Boukheddaden, and F. Varret, Macroscopic nucleation phenomena in continuum media with long-range interactions, Sci. Rep. **1**, 162 (2011).

[44] C. Enachescu, L. Stoleriu, A. Stancu, and A. Hauser, Model for Elastic Relaxation Phenomena in Finite 2d Hexagonal Molecular Lattices, Phys. Rev. Lett. **102**, 257204 (2009).

[45] K. Affes, H. Fourati, A. Slimani, and K. Boukheddaden, Effects of high-spin-low-spin lattice misfit on the nucleation and propagation velocities of elastic interfaces in cooperative spin-crossover solids, J. Phys. Soc. Jpn. **88**, 124701 (2019).

[46] D. Chiruta, C.-M. Jureschi, J. Linares, Y. Garcia, and A. Rotaru, Lattice architecture effect on the cooperativity of spin transition coordination polymers, J. Appl. Phys. **115**, 053523 (2014).

[47] T. Kawamoto and S. Abe, Thermal hysteresis loop of the spin-state in nanoparticles of transition metal complexes: Monte Carlo simulations on an Ising-like model, Chem. Commun. 3933 (2005), doi: 10.1039/B506643C.

[48] A. Slimani, K. Boukheddaden, and K. Yamashita, Effect of intermolecular interactions on the nucleation, growth, and propagation of like-spin domains in spin-crossover materials, Phys. Rev. B **92**, 014111 (2015).

[49] A. Slimani, K. Boukheddaden, F. Varret, M. Nishino, and S. Miyashita, Properties of the low-spin high-spin interface during the relaxation of spin-crossover materials, investigated through an electro-elastic model, J. Chem. Phys. **139**, 194706 (2013).

[50] R. Traiche, M. Sy, H. Oubouchou, G. Bouchez, F. Varret, and K. Boukheddaden, Spatiotemporal observation and modeling of remarkable temperature scan rate effects on the thermal hysteresis in a spin-crossover single crystal, J. Phys. Chem. C **121**, 11700 (2017).

[51] M. Paez-Espejo, M. Sy, F. Varret, and K. Boukheddaden, Quantitative macroscopic treatment of the spatiotemporal properties of spin crossover solids based on a reaction diffusion equation, Phys. Rev. B **89**, 024306 (2014).

[52] A. Slimani, F. Varret, K. Boukheddaden, D. Garrot, H. Oubouchou, and S. Kaizaki, Velocity of the high-spin low-spin interface inside the thermal hysteresis loop of a spin-crossover crystal, via photothermal control of the interface motion, Phys. Rev. Lett. **110**, 087208 (2013).

[53] See Supplemental Material at http://link.aps.org/supplemental/10.1103/PhysRevB.101.224101 for further plots of the thermal dependence of the red, green, and blue optical densities of crystals **1a**, **1b**, **2**, and **3**; for the comparison between OM and x-ray data of all studied crystals; and for the time dependence of the three red, green, and blue OD measured at the probed regions for the four crystals.

[54] S. Decurtins, P. Gütlich, C. P. Köhler, H. Spiering, and A. Hauser, Light-induced excited spin state trapping in a transition-metal complex: The hexa-1-propyltetrazole-iron (II) tetrafluoroborate spin-crossover system, Chem. Phys. Lett. **105**, 1 (1984).

[55] K. Boukheddaden and M. Sy, Direct optical microscopy observation of photo-induced effects and thermal relaxation in a spin crossover single crystal, Curr. Inorg. Chem. **6**, 40 (2016).

[56] E. Milin, V. Patinec, S. Triki, E.-E. Bendeif, S. Pillet, M. Marchivie, G. Chastanet, and K. Boukheddaden, Elastic frustration triggering photoinduced hidden hysteresis and multistability in a two-dimensional photoswitchable hofmann-like spin-crossover metal organic framework, Inorg. Chem. **55**, 11652 (2016).

[57] G. Chastanet, C. Desplanches, C. Baldé, P. Rosa, M. Marchivie, and P. Guionneau, A critical review of the T(LIESST) temperature in spin crossover materials - what it is and what it is not, Chem. Squared **2**, 2 (2018).